



Observations of the Fading Outburst System L1251 VLA 6

AVA NEDERLANDER ^{1,2} AND JACOB A. WHITE ²

¹*Astronomy Department and Van Vleck Observatory, Wesleyan University, Middletown, CT 06459, USA*

²*The National Radio Astronomy Observatory, 520 Edgemont Road Charlottesville, VA 2290, USA*

ABSTRACT

Young protostars that undergo episodic accretion can provide insight into the effects of stellar evolution and impact on their circumstellar environments. L1251 VLA 6 is a four component protostar system with one of those being a fading outbursting protostar. Here we examine structure in the disk around L1251 VLA 6 at a frequency of 33 GHz with the Very Long Array (VLA). Given the rarity of YSOs undergoing this type of accretion, L1251 VLA 6 can provide insight into the fading post-outburst process. To constrain the disk structure, we adopt a modeling approach specifically taking the protoplanetary disk density profile equations laid out in [Andrews et al. \(2009\)](#) and then follows the same technique as in [White et al. \(2020\)](#) that uses an MCMC approach to constrain the most probable values. This model then combined with a parametric ray-tracing code to generate synthetic model images of an axisymmetric disk with an MCMC fitting algorithm, allowing us to characterize the radial distribution of dust in the system. The results of our MCMC fit shows that the most probable values for the mass and radius are more consistent with Class I. We find that the mass of the disk to be 0.070, consistent with calculated values. Additionally, we investigate the reasoning for the accretion outburst, which we determine is not caused by gravitational instability.

1. INTRODUCTION

The star formation process begins when in the dense regions of interstellar molecular clouds in which a gravitational collapse that causes gas and dust to heat up and begin forming young stellar objects (YSOs). The rotation of the collapsing cloud core produces accretion disks, which can add mass to the protostar. Mass buildup in stars can be accelerated by episodic accretion in young stellar objects. Theoretical considerations (e.g., [Vorobyov & Basu 2015](#)) suggest that Sun-like stars build up their mass during periods of significantly enhanced accretion (i.e., episodic accretion). Episodic accretion can play a crucial role in the evolution of circumstellar disks, and it is considered to have an impact on planet formation. Outbursts have been shown to potentially change the chemistry and mineralogy of the surrounding circumstellar disk ([Ábrahám et al. 2009](#); [Rab et al. 2017](#)); could spur the growth of small solids through, e.g., evaporation and recondensation from a rapid evolution of the ice line ([Cieza et al. 2018](#)); and offer a potential solution to the luminosity problem ([Hartmann & Kenyon 1996](#)).

While it is possible that most Sun-like stars undergo several outbursts during their pre-main sequence evolution ([Audard et al. 2014](#)), there are very few known young stars that experience accretion outbursts (Class 0 and Class I YSOs; [Greene et al. \(1994\)](#)). Those discovered were originally observed in the prototypes FU Orionis and EX Lupi. Mechanisms of mass accumulation and disk heating, leading to accretion bursts, are discussed in several theoretical papers (e.g., [Bell & Lin 1994](#); [Bell et al. 1995](#); [Vorobyov & Basu 2006](#); [Zhu et al. 2009](#); [Bae et al. 2014](#)). Episodic outbursts are caused by matter accumulation in the inner disk region as a result of angular momentum rearrangements in the outer disk caused by gravitational instabilities (GI), as proposed in [Zhu et al. \(2009\)](#). The inner disk heating as a result of the rising ionization initiates instabilities, including magnetorotational and thermal, which propel the gas to accrete from the disk to the star ([Bell & Lin 1994](#)).

FU Orionis type stars, which we will refer to as FUors, are embedded objects and can exhibit a rapid increase in magnitude ($\Delta V > 5$) lasting 10s to 100s of years. EX Lupi type stars, which we will refer to as EXors, are typically observed to no longer be embedded and have smaller and shorter lived outbursts. The increase in magnitude of which is due to an increase in the accretion, further raising the luminosity of the innermost region of the protostar and surrounding areas outside of the protostar. An ALMA survey presented in [Kóspál et al. \(2021\)](#) found that FUors tend to be more compact and massive than other disks.

2MASS 22352345+7517076, hereto refer as L1251 VLA 6, is an embedded eruptive YSO. It is associated with IRAS 22343+7501, a protostellar source embedded in the molecular cloud Lynds 1251. [Rosvick & Davidge \(1995\)](#) identified a cluster of five near-infrared sources associated with IRAS 22343+7501 (RD95 A, B, C, D, and E). The cluster is a source of several molecular outflows ([Sato & Fukui 1989](#); [Nikolić et al. 2003](#); [Kim et al. 2015](#)), the Herbig–Haro jet HH 149 ([Balazs et al. 1992](#)), and radio continuum jet sources (VLA 6, 7, and 10, ([Reipurth et al. 2004](#))). L1251 VLA 6 is a four component system with stars RD95A, RD95B, and RD95C referred to as A, B, and C respectively with the FUor referred to as D.

L1251 VLA 6 began a dramatic brightening at mid-IR wavelengths sometime between the IRAS (1983), Akari (2006), and Wide-field Infrared Survey Explore (WISE) surveys that were launched between 1983, 2006, and 2009 ([Onozato et al. 2015](#)). Over the course of a 35-yr period, D experienced quiescence in 1983–1996, slow dust accumulation in 1999–2004, and an outburst in 2007–2010 ([Kun et al. 2019](#)). Recent work has shown that L1251 VLA 6 underwent an energetic accretion outburst between 2007 and 2017, with the central star likely being a YSO with a mass of $1.6 - 2.0 M_{\oplus}$, and having a bolometric luminosity that increased from $32 L_{\odot}$ to $165 L_{\odot}$ between 1983 and 2010 ([Kun et al. 2019](#)). The peak accretion rate was slightly more than $10^{-4} M_{\oplus} \text{ yr}^{-1}$, typical of an FUor-type outburst. One possible explanation of the outburst, supported by the observed timescales, is that a $\sim 318 M_{\oplus}$ buildup of material formed from GI and was slowly accreted onto the star ([Kuffmeier et al. 2018](#)). However, the exact cause of the outburst, and indeed the underlying mechanism of outbursts in general, is not well constrained. In order to build an accurate profile of outbursting protostars, detailed observations with broad spectral coverage, broad spatial scales, and covering the epochs of before, during, and after outburst are imperative.

L1251 VLA 6 presents a valuable opportunity to observe a young four-component star system and the underlying effects these stars potentially have on each other, one of which experiencing an accretion outburst. Given the rarity of YSOs undergoing this type of accretion, L1251 VLA 6 can provide insight into the fading post-outburst process.

In this paper, we describe the new observational data in Section 2, look at results in Section 3, examine disk parameters and constraints in Section 4, discussion in Section 5, and summary and conclusion in Section 6.

2. OBSERVATIONS

This analysis uses data from NSF’s Karl G. Jansky Very Large Array (VLA) obtained on 2019 November 08 (ID 19B-088, PI White). The observations were centered on L1251 VLA 6 using J2000 coordinates $RA = 22^{\text{hr}} 35^{\text{min}} 23.46^{\text{s}}$ and $\delta = +75^{\circ} 17' 7''.60$ and accounted for proper motion. The data used 27 antennas in the D configuration with baselines ranging from 0.035 – 1.03 km. The total time on-source was 831 s.

The observations used a Ka Band tuning setup with 4×2.048 GHz basebands and rest frequency centers of 28.976 GHz, 31.024 GHz, 34.976 GHz, and 37.024 GHz, yielding an effective frequency of 33 GHz (9.1 mm). The raw data was reduced and calibrated using the *CASA* 6.1.2-7 pipeline ([McMullin et al. 2007](#)), which included bandpass, flux, and phase calibrations. Quasar J0019+7327 was used for phase and bandpass calibrations and quasar 0542+498=3C147 was used as a flux calibration source. The absolute flux calibration of the VLA at these frequencies is typically $\sim 5\%$. The pipeline calibrated data was inspected in *CASA* and additional flagging was performed to account for radio frequency interference (RFI). All the significantly impacted channels and time bins were flagged and the pipeline was ran again.

The final calibrated dataset was imaged with a natural weighting and cleaned using *CASA*’s *CLEAN* algorithm down to a threshold of $1.5 \times \sigma_{RMS}$. The observations achieve a sensitivity of $19 \mu\text{Jy beam}^{-1}$ as measured in the CLEANed image. The size of the resulting synthesized beam is 3.94×2.07 at a position angle of -68.3° .

Table 1. Ka Band Observations

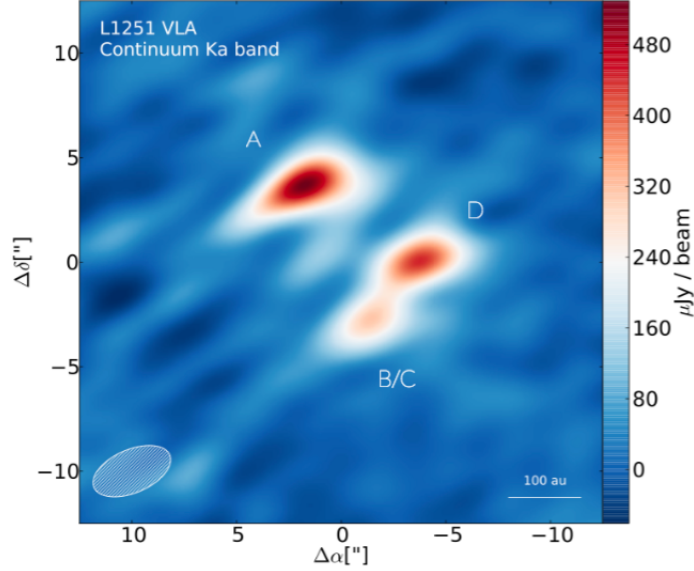
Date	Frequency (GHz)	Flux (μJy)	Observing Time (hr)
2019 November 08	33.0 (Ka Band)	445.6	0.5

3. RESULTS

Figure 1 shows a naturally weighted image of the combined data set generated using the *CASA* task *tclean*. We used *CASA*’s *imfit* tool to derive basic parameters such as coordinates, sizes, inclinations, position angles, and fluxes which

Table 2. 2D Gaussian Model Fitting

	A	B/C	D
Position Angle ($^{\circ}$)	117.0	-	102.5
Peak Flux (μJy)	522.0	314.2	442.0

**Figure 1.** Continuum image of the Ka band resolved with source components A, B/C, and D visible. The hatched ellipse in the lower left corner represents the size and orientation of the synthesized beam.**Table 3.** L1251 VLA 6 mass calculations (M_{\oplus}) with kappa ($k = 0.02896 (m^2)/kg$) varying Temperature (K)

	disk mass (M_{\oplus})
T = 30	0.1186
T = 50	0.0704
T = 70	0.0501
T = 90	0.0388

Table 4. L1251 VLA 6 mass calculations (M_{\oplus}) varying density (kg/m^3) and Temperature (K)

	d = 1000	d = 1500	d = 2000	d = 2500	d = 3000
T = 30	0.0386	0.0579	0.0772	0.0966	0.1159
T = 50	0.0229	0.0344	0.0459	0.0573	0.0688
T = 70	0.0163	0.0245	0.0326	0.0407	0.0489
T = 90	0.0126	0.0190	0.0253	0.0316	0.0379

are presented in Table 1. This enabled us to find best-fit 2D Gaussian models for each source component, which are presented in Table 2. The source components B/C could not have an upper limit on its sizes determined.

3.1. Dust Masses

At millimeter wavelengths, protoplanetary disks become optically thin with the exception of the core regions of particularly massive systems (Cieza et al. 2018). This means that the majority of dust grains are responsible for the observed emission, and the total flux is closely related to the total mass of small grains size. The following formula can be used to determine the dust masses of protoplanetary disks using millimeter fluxes:

$$M_{\text{dust}} = \frac{d^2 F_\nu}{\kappa_\nu B_\nu(T)}. \quad (1)$$

where d is the distance to the target, F_ν is the flux density, κ_ν is the dust opacity as used in Cieza et al. (2018), and $B_\nu(T)$ is the Planck function evaluated at a dust temperature of T (e.g., (Andrews et al. 2013)). Table 3 presents our results.

As another estimate for calculating dust mass, we use the formula focusing on emission that accounts for the internal density and the solid angle of a single grain:

$$M_{\text{dust}} = \frac{4}{3} \pi s^3 \rho \frac{F_\nu}{B_\nu(T) \Omega_s} \quad (2)$$

where ρ is the internal density and Ω_s is the solid angle of a single grain. Table 4 presents our results.

By comparing the two results for Equation 1 and Equation 2, we are able to determine how varying the density and temperature, in addition to other parameters, can affect the potential mass of the disk. It is apparent that varying temperature and density can result in results that vary by a factor of 2. Seeing these results gives us a good indication on what we can expect from the final disk mass calculation and the exact implications for that could be. It is evident that in Table 3, the disk mass decreases as the temperature increases. The same scenario similarly appears in Table 4 in addition to the disk mass increasing as the density increases.

Now that we have been able to determine a best guess analysis of the disk mass and the physical radius in au, we are able to begin generating disk models in RADMC-3D that can be compared to the images.

3.2. Spectral Index

We measured the spectral index α of our target, L1251 VLA 6, by constructing comparisons from the two continuum spectral windows separately with v_1 and v_2 , and measuring the targets' fluxes (F) at these two frequencies. Then we calculated α using:

$$\alpha = \frac{\log(F_{v_1}) - \log(F_{v_2})}{\log(v_1) - \log(v_2)} \quad (3)$$

and its uncertainties σ with:

$$\sigma = \left(\frac{1}{\ln(v_1) - \ln(v_2)} \right)^2 \left(\frac{\sigma_{v_1}^2}{F_{v_1}^2} + \frac{\sigma_{v_2}^2}{F_{v_2}^2} \right) \quad (4)$$

The calculated indices are from JCMT/SCUBA-2 2014, SMA 2007 Oct 17, and the Very Large Array Sky Survey (VLASS) as presented in Kun et al. (2019). The indices are also calculated for the Ka band observations and also 10 GHz X band observations (ID 20B-096, PI White). We found the spectral index uncertainties from JCMT to SMA is 5.670 ± 0.018 , SMA to 33GHz 2.018 ± 0.0053 , 33GHz to 10GHz is -0.379 ± 0.0140 , and 10GHz to VLASS is 1.912 ± 0.0138 . We are able to see how the spectral index from JCMT to SMA is much larger by a multiple of 2 than the other indices. This could be the result of jet emissions that is accounted for at higher wavelengths. Using the `radmc3dPy` package, we were able to produce Figure 2. Emission is not expected from the disk at 10 GHz as visible in Figure 2 as the spectrum profile is faint at that frequency.

4. ANALYSIS

In this section, we analyze the data from the L1251 VLA 6 emission to characterize in detail the spatial distribution of dust in the system. We adopt a modeling approach specifically taking the protoplanetary disk density profile equations laid out in Andrews et al. (2009) and then follows the same technique as in White et al. (2020) that uses an MCMC approach to constrain the most probable values. This model then combined with a parametric ray-tracing code to generate synthetic model images of an axisymmetric disk with an MCMC fitting algorithm, allowing us to characterize the radial distribution of dust in the system.

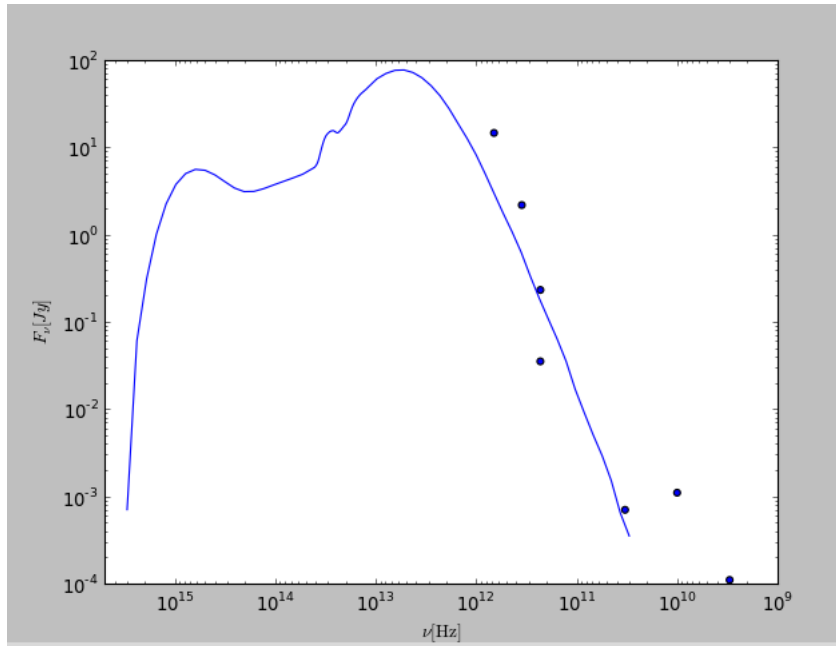


Figure 2. Spectral energy distribution displaying values from the JCMT/SCUBA-2 2012–2014, SMA 2007 Oct 17, 33GHz, 10GHz, and VLASS data as presented in Kun et al. (2019).

4.1. Radiative Transfer Modeling

We adopted a radiative transfer model fitting approach in Dullemond et al. (2012) in order to constrain the disk parameters of source component D. This approach gives us a more accurate model than a simple Gaussian as presented in Figure 1. To obtain the physical parameters of the spatially resolved disks, we use the RADMC-3D code (Dullemond et al. 2012) to build radiative transfer models with the Python interface radmc3dPy¹.

The density profile of a trial protoplanetary disk model is given by:

$$\rho = \frac{\Sigma(r, \phi)}{H_p \sqrt{2\pi}} \exp\left(-\frac{z^2}{2H_p^2}\right), \quad (5)$$

where Σ is the surface density profile, and H_p is the pressure scale height. The surface density profile includes a power-law inner disk and an exponential out tapering (Andrews et al. 2009):

$$\Sigma(r) = \Sigma_0 \left(\frac{r}{R_c}\right)^{-\gamma} \exp\left\{-\left(\frac{r}{R_c}\right)^{2-\gamma}\right\}, \quad (6)$$

where R_c is the characteristic radius of the disk, γ is the power-law exponent of the radial surface density profile, and Σ_0 is a surface density normalization factor with:

The pressure scale height is defined as:

$$H_p = h_c \left(\frac{r}{R_c \text{ au}}\right)^{1+\psi}, \quad (7)$$

where h_c is the ratio of the pressure scale height over radius at R_c and ψ is the degree of flaring for the disk.

To generate realistic dust absorption and scattering properties, we followed the same approach as White et al. (2020) and generated the RADMC-3D input opacity files with the OpacityTool² program (Toon & Ackerman 1981; Woitke et al. 2016). This program calculates dust opacities by using a volume mixture of 60% amorphous silicates (e.g., Dorschner et al. 1995), 15% amorphous carbon (e.g. Zubko et al. 1996), and a 25% porosity. Bruggeman mixing is used to

¹ <https://www.ita.uni-heidelberg.de/dullemond/software/radmc-3d/manualrmcpy/index.html>

² The OpacityTool Software was obtained from <https://dianaproject.wp.st-andrews.ac.uk/data-results-downloads/fortran-package/>

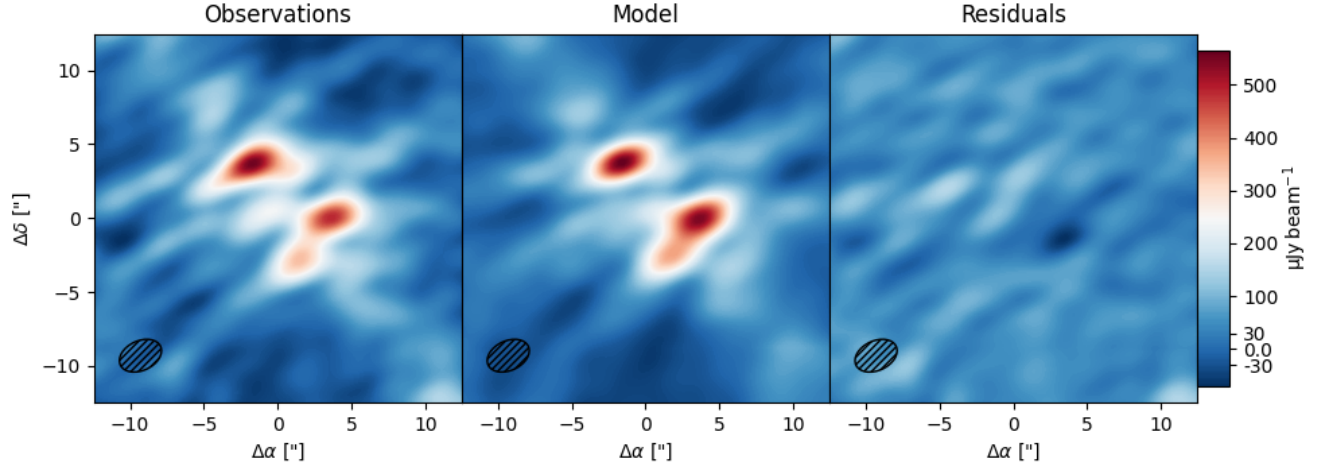


Figure 3. (Left) Naturally weighted VLA image of the L1251 VLA 6 system. (Center) Model image showing the most-probable model. (Right) Residual image after subtracting the model from the data.

calculate an effective refractory index and a distribution of hollow spheres with a maximum hollow ratio of 0.8 (Min et al. 2005) is included to avoid Mie theory scattering artifacts. The disk is populated by $0.1 - 15000 \mu\text{m}$ grains following a power-law size distribution of $s^{-3.5}$. The gas to dust mass ratio is also calculated with the mass values constrained and reported are the total mass values.

4.2. Modeling Formalism

To converge on the best fit model, we use a Metropolis-Hastings Markov Chain Monte Carlo (MCMC) model fitting approach, similarly approached as in White et al. (2020). The free parameters considered in the modelling are: stellar radius, the total disk mass, M_{disk} , degree of disk flaring, Ψ , characteristic radius, R_c , power law exponent of the surface density profile, γ , and scale height ratio, h_c . Given the detailed calculation in RADMC-3D, a continuum image is then produced and projected to a trial inclination and position angle. The trial model is then attenuated by the primary beam and convolved with the synthetic beam for the observational setup.

To assess the likelihood of a given model, a χ^2 is calculated as

$$\chi^2 = \frac{(Data - Model)^2}{\sigma^2}, \quad (8)$$

where σ is the observed σ_{rms} for a given observation multiplied by the synthetic beam size in pixels (see Booth et al. (2016)).

A trial model is accepted if a random number drawn from a uniform distribution $[0,1]$ is less than α , where

$$\alpha = \min(e^{\frac{1}{2}(\chi_i^2 - \chi_{i+1}^2)}, 1). \quad (9)$$

For source component D, we ran 100 chains with 1000 links each (minus 100 burn-in). The most probable values are summarized in Table 5. The 95% credible regions are also presented, indicated from the posterior distributions (Figure 7), provides uncertainties for the MCMC fit and corresponds roughly to 2σ uncertainties. Figure 1 shows the data image (left) compared with the best-fit model (center), and the residuals (right). Figure 4 shows a 2D slice of the disk's density structure as a function of radius. Disk is flared due to the outburst heating up the disk which increases the vertical mixing and therefore ends up making the disk thicker. The temperature contour lines correspond to the snowlines. These move outward from the outburst because the central effective temperature went up.

5. DISCUSSION

The FUor disks' larger and compact structure can reveal the source of the episodic accretion that causes the outbursts. While the exact mechanisms that drive increased disk material accretion onto the protostar are unknown, it could be a result of the disk becoming gravitationally unstable, possibly in conjunction with a magnetorotational

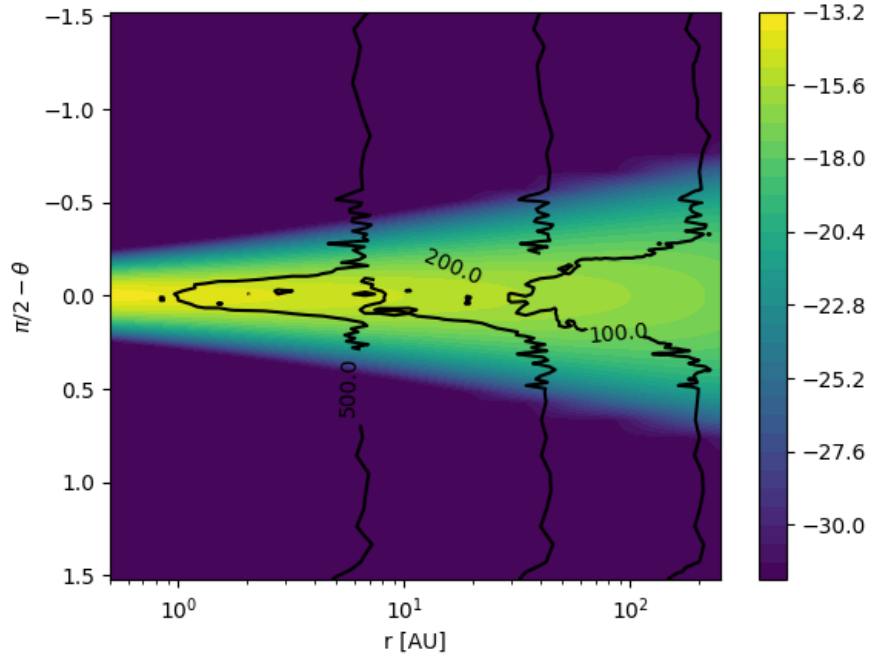


Figure 4. 2D slice of the disk’s density structure. Disk is flared due to the outburst heating up the disk which increases the vertical mixing and therefore ends up making the disk thicker.

Table 5. MCMC Fitting Results

Parameter	D		A	
	Best Fit	95% regions	Best Fit	95% regions
$M_{disk} (M_{\odot})$	0.070	[0.031, 0.2]	0.103	[0.052, 0.301]
R_c (au)	260.0	[110, 340]	365.8	[200, 440]
γ	-0.110	[-1.78, 1.1]	-0.992	[-1.9, 0.99]
h_c (au)	0.130	[0.014, 0.08]	0.103	[0.04, 0.08]
$R_{star} (R_{\odot})$	4.5	[0.81, 7.9]	4^a	
Ψ	0.250	[0.011, 0.48]	0.204	[0.11, 0.5]

NOTE—^a R_{star} is a fixed parameter for source component A, so there are no 95% credible regions.

instability. Gravitational instability is largely responsible for outbursts. There are multiple metrics to calculate the gravitational instability, the more detailed of which is using Toomre’s Q parameter. Gravitational instability occurs if the value of Toomre’s Q parameter is $Q = c_s \Omega / \pi G \Sigma \lesssim 1.4$, where c_s is the sound speed, Ω is the epicyclic frequency for a Keplerian disk, and Σ is the column density at a given radius in the disk. The gravitational instability plot and results is presented in Figure 5. We found that L1251 VLA 6 is not gravitationally unstable, inconsistent with the other 65% FUor disks that were examined in Kóspál et al. (2021). This implies that there are other underlying causes for the enhanced accretion. According to Hartmann & Kenyon (1996), mass is added onto the central star so rapidly that the X-wind region is probably crushed out of existence, implying that the strong outflows that still occur during these outbursts must be caused by an extended disk wind. Recent findings also indicate that the process of outburst accretion is probably episodic in the form of accretion bursts, possibly caused by disk fragmentation (Caratti o Garatti

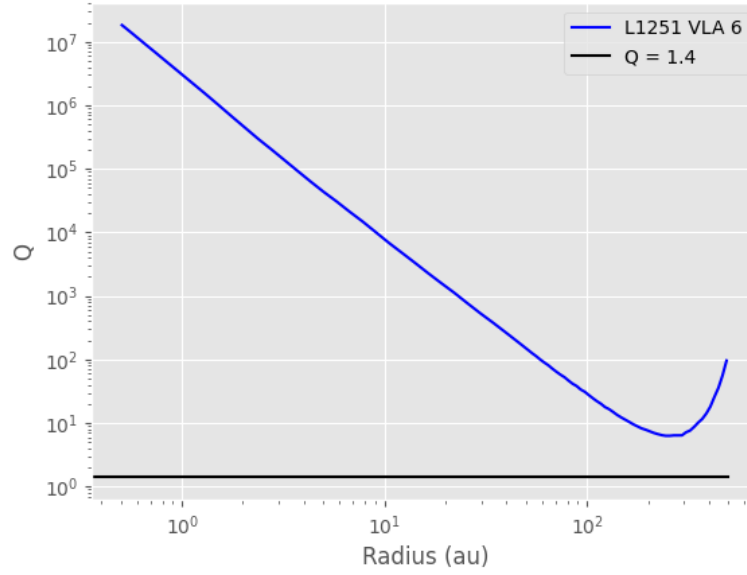


Figure 5. Gravitational Instability plot with the upper limit of Toomre’s Q parameter of 1.4 represented by the black line. The calculations for L1251 VLA 6 are represented by the blue line.

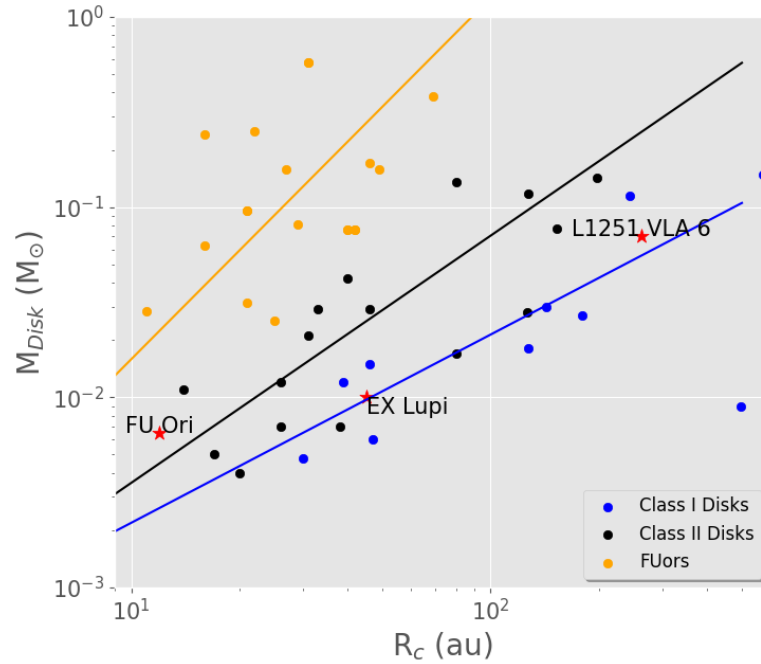


Figure 6. Total disk mass (in M_{\odot}) as a function of characteristic radii. The orange points are the FUors presented in Pérez et al. (2010); Cieza et al. (2018); Pérez et al. (2020); Kóspál et al. (2021). The black points are T Tauri disks from Andrews et al. (2009). The blue points are Class I disks from Sheehan & Eisner (2014). FU Ori, Ex Lupi, and L1251 VLA 6 are labeled.

et al. 2017). Further investigation will have to be conducted in order to determine the cause of the outburst in this system.

The results of our MCMC fit shows that the most probable values for the mass and radius are more consistent with Class I and opposed to Class 0. For our observations, the flux calibration was off and thus may have affected our results. In Figure 6, we show the total disk mass as a function of the characteristic radius. This mass-radius plot is adopted from Kóspál et al. (2021) and show Class I Disks, Class II Disks, and FUors All the disks included in that plot were modeled in a similar fashion with RADMC-3D and radio data as there are many more disks than what is included but most do not constrain the parameters with the same approach. The orange points are the FUors presented in Kóspál et al. (2021). The yellow points are FUors from Pérez et al. (2020). The black points are T Tauri disks from Andrews et al. (2009). The blue points are Class I disks from Sheehan & Eisner (2014). Then we note on top of that FU Ori, EX Lupi, and L1251 to see how they look comparatively to each other. It is evident that FUor disks tend to be more massive and more compact than the other two categories of disks. Also to compare, the radius of L1251 VLA 6 is much larger and wider than expected.

The resulting disk mass of 0.070 from the MCMC fitting, in comparison to the dust calculations in Section 3.1 is consistent. The disk mass values closely resembles the resulting value when temperature is set to 50 K in Equation 1. The value is also similarly consistent when temperature is 50 K and density is $3,000 \text{ kg/m}^3$ in Equation 2. This value also resembles closely to when the temperature is 30 K and density is $2,000 \text{ kg/m}^3$. The exact values of which are presented in Table 3 and Table 4.

For future analysis, we will look at 10GHz X Band observations in order to look at the jet emissions. Continuing to run MCMC in order to make better constraints on the disks. Higher resolution data, especially to spatially resolve source components B and C.

6. SUMMARY AND CONCLUSION

We present radio observational data of the L1251 VLA 6 system. During the Ka band observation, protostar source component D underwent a fading outburst. Overall, we show key observations and results of L1251 VLA 6. We were able to constrain parameters for source component D using MCMC.

We found that the resulting disk mass of 0.070 from the MCMC fitting, in comparison to the dust calculations in Section 3.1 is consistent. The disk mass values closely resembles the resulting value when temperature is set to 50 K in Equation 1. The value is also similarly consistent when temperature is 50 K and density is $3,000 \text{ kg/m}^3$ in Equation 2. This value also closely resembles to when the temperature is 30 K and density is $2,000 \text{ kg/m}^3$.

We found the spectral index uncertainties from JCMT to SMA is 5.670 ± 0.018 , SMA to 33GHz 2.018 ± 0.0053 , 33GHz to 10GHz is -0.379 ± 0.0140 , and 10GHz to VLASS is 1.912 ± 0.0138 . We are able to see how the spectral index from JCMT to SMA is much larger by a multiple of 2 than the other indices. This could be the result of jet emissions that is accounted for at higher wavelengths. Using the `radmc3dPy` package, we were able to produce Figure 2. Emission is not expected from the disk at 10 GHz as visible in Figure 2 as the spectrum profile is faint at that frequency.

We also have been able to determine that gravitational instability is not a cause of the accretion outburst as the resulting values were larger than 1.4, which is the upper limit for Toomre's Q parameter.

The results of our MCMC fit shows that the most probable values for the mass and radius are more consistent with Class I than to Class 0. This confirmation is important to our understanding of the properties of the fading outburst system.

ACKNOWLEDGMENTS

A.N. is supported by the Research Experiences for Undergraduates program of the National Science Foundation. The National Radio Astronomy Observatory is a facility of the National Science Foundation operated under cooperative agreement by Associated Universities, Inc.

This paper makes use of the following VLA data: VLA/2019-00-036 and VLA/20B-096.

Software: `Astropy` (Astropy Collaboration et al. 2018), `CASA` (McMullin et al. 2007), `Matplotlib` (Hunter 2007), `NumPy` (van der Walt et al. 2011), `Pandas` (Wes McKinney 2010), `RADMC-3D` (Dullemond et al. 2012).

APPENDIX

In this Appendix, we show the Posterior distributions for the MCMC chains for the D and A source components (Figure 7 and Figure 8).

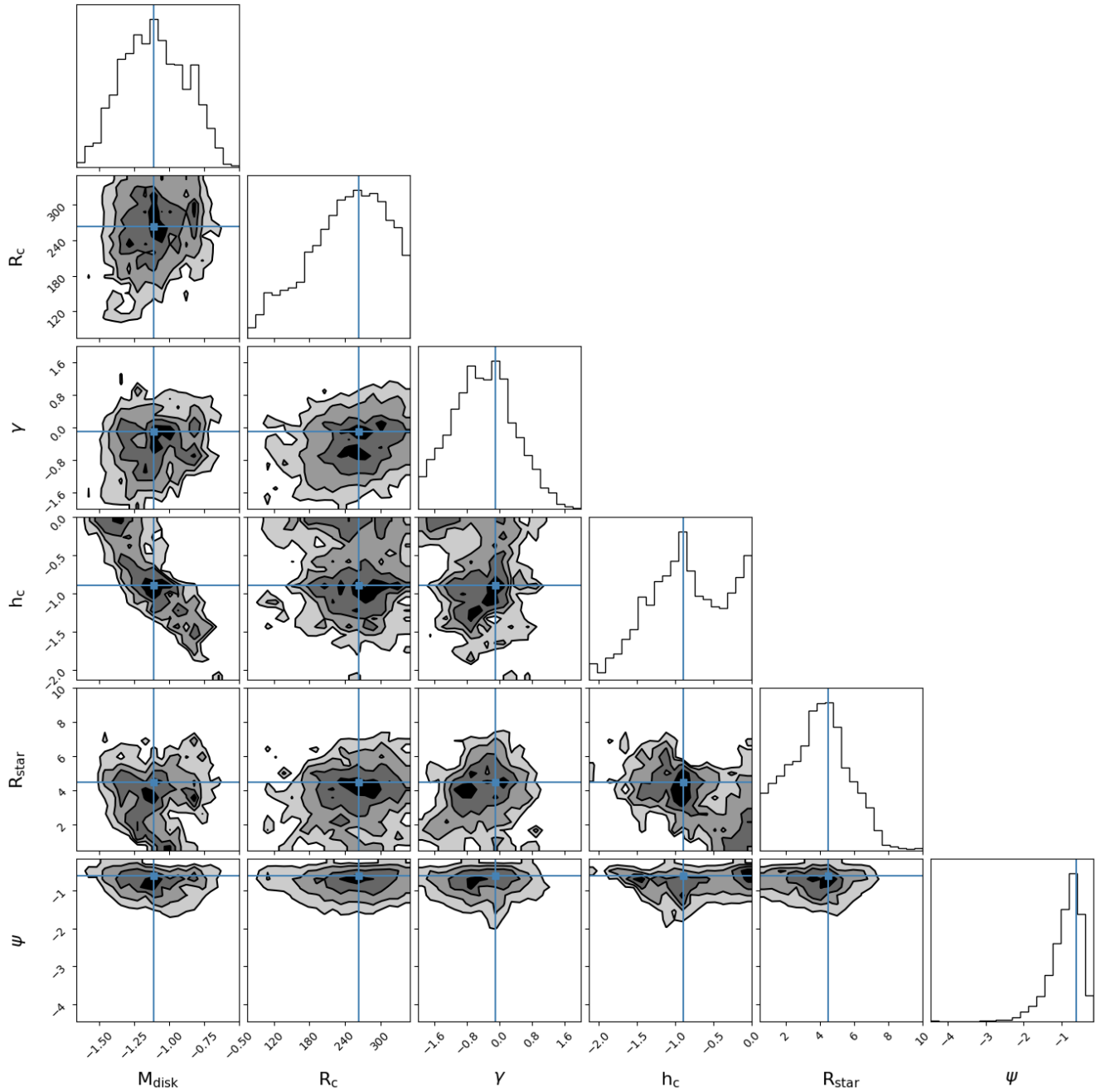


Figure 7. Posterior distributions for the MCMC chains for the source component D after removing burn-in. Histograms for each parameter are plotted at the top of the corresponding column, while the plots for the rest of the grid show the distribution of walkers across slices through parameter space for the corresponding pair of parameters. The best-fit value for each parameter is plotted with a blue line.

REFERENCES

Ábrahám, P., Juhász, A., Dullemond, C. P., et al. 2009,
Nature, 459, 224

Andrews, S. M., Rosenfeld, K. A., Kraus, A. L., & Wilner,
D. J. 2013, ApJ, 771, 129

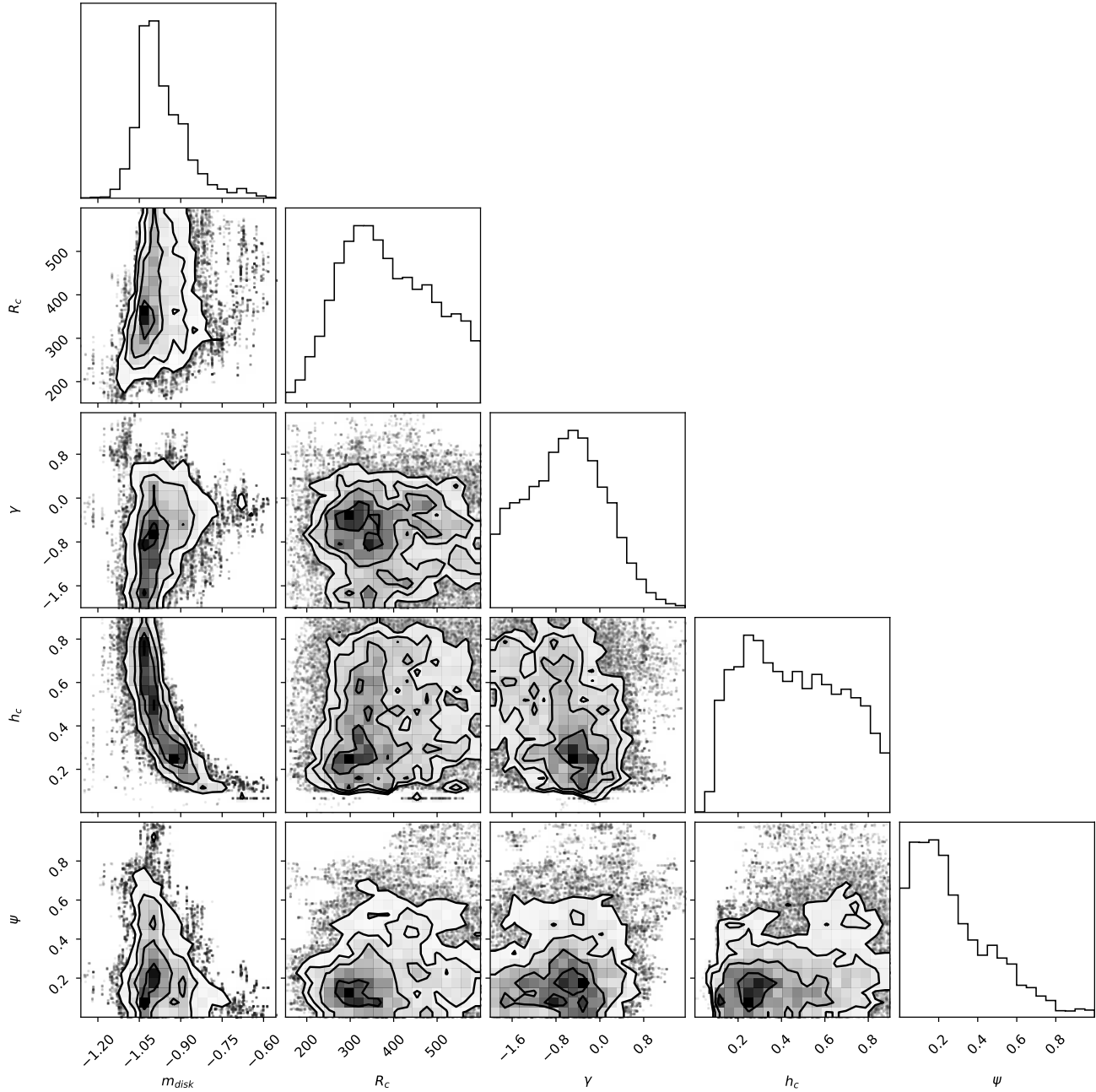


Figure 8. Posterior distributions for the MCMC chains for the source component A after removing burn-in. Histograms for each parameter are plotted at the top of the corresponding column, while the plots for the rest of the grid show the distribution of walkers across slices through parameter space for the corresponding pair of parameters.

Andrews, S. M., Wilner, D. J., Hughes, A. M., Qi, C., & Dullemond, C. P. 2009, *ApJ*, 700, 1502

Astropy Collaboration, Price-Whelan, A. M., Sipőcz, B. M., et al. 2018, *AJ*, 156, 123

Audard, M., Ábrahám, P., Dunham, M. M., et al. 2014, in *Protostars and Planets VI*, ed. H. Beuther, R. S. Klessen, C. P. Dullemond, & T. Henning, 387

Bae, J., Hartmann, L., Zhu, Z., & Nelson, R. P. 2014, *ApJ*, 795, 61

Balazs, L. G., Eisloffel, J., Holl, A., Kelemen, J., & Kun, M. 1992, *A&A*, 255, 281

Bell, K. R., & Lin, D. N. C. 1994, *ApJ*, 427, 987

Bell, K. R., Lin, D. N. C., Hartmann, L. W., & Kenyon, S. J. 1995, *ApJ*, 444, 376

- Booth, M., Jordán, A., Casassus, S., et al. 2016, *MNRAS*, 460, L10
- Caratti o Garatti, A., Stecklum, B., Garcia Lopez, R., et al. 2017, *Nature Physics*, 13, 276
- Cieza, L. A., Ruíz-Rodríguez, D., Perez, S., et al. 2018, *Monthly Notices of the Royal Astronomical Society*, 474, 4347
- Dorschner, J., Begemann, B., Henning, T., Jaeger, C., & Mutschke, H. 1995, *Astronomy and Astrophysics*, 300, 503
- Dullemond, C. P., Juhasz, A., Pohl, A., et al. 2012, *RADMC-3D: A multi-purpose radiative transfer tool*, ascl:1202.015
- Greene, T. P., Wilking, B. A., Andre, P., Young, E. T., & Lada, C. J. 1994, *ApJ*, 434, 614
- Hartmann, L., & Kenyon, S. J. 1996, *ARA&A*, 34, 207
- Hunter, J. D. 2007, *Computing in Science and Engineering*, 9, 90
- Kim, J., Lee, J.-E., Choi, M., et al. 2015, *ApJS*, 218, 5
- Kóspál, Á., Cruz-Sáenz de Miera, F., White, J. A., et al. 2021, arXiv e-prints, arXiv:2106.14409
- Kuffmeier, M., Frimann, S., Jensen, S. S., & Haugbølle, T. 2018, *MNRAS*, 475, 2642
- Kun, M., Ábrahám, P., Acosta Pulido, J. A., Moór, A., & Prusti, T. 2019, *MNRAS*, 483, 4424
- McMullin, J. P., Waters, B., Schiebel, D., Young, W., & Golap, K. 2007, in *Astronomical Society of the Pacific Conference Series*, Vol. 376, *Astronomical Data Analysis Software and Systems XVI*, ed. R. A. Shaw, F. Hill, & D. J. Bell, 127
- Min, M., Hovenier, J., & de Koter, A. 2005, *Astronomy & Astrophysics*, 432, 909
- Nikolić, S., Johansson, L. E. B., & Harju, J. 2003, *A&A*, 409, 941
- Onozato, H., Ita, Y., Ono, K., et al. 2015, *PASJ*, 67, 39
- Pérez, L. M., Lamb, J. W., Woody, D. P., et al. 2010, *The Astrophysical Journal*, 724, 493
- Pérez, S., Hales, A., Liu, H. B., et al. 2020, *ApJ*, 889, 59
- Rab, C., Güdel, M., Padovani, M., et al. 2017, *A&A*, 603, A96
- Reipurth, B., Rodríguez, L. F., Anglada, G., & Bally, J. 2004, *AJ*, 127, 1736
- Rosvick, J. M., & Davidge, T. J. 1995, *PASP*, 107, 49
- Sato, F., & Fukui, Y. 1989, *ApJ*, 343, 773
- Sheehan, P. D., & Eisner, J. A. 2014, *ApJ*, 791, 19
- Toon, O. B., & Ackerman, T. 1981, *Applied Optics*, 20, 3657
- van der Walt, S., Colbert, S. C., & Varoquaux, G. 2011, *Computing in Science and Engineering*, 13, 22
- Vorobyov, E. I., & Basu, S. 2006, *ApJ*, 650, 956
- . 2015, *ApJ*, 805, 115
- Wes McKinney. 2010, in *Proceedings of the 9th Python in Science Conference*, ed. Stéfan van der Walt & Jarrod Millman, 56 – 61
- White, J. A., Kóspál, Á., Hughes, A., et al. 2020, *The Astrophysical Journal*, 904, 37
- Woitke, P., Min, M., Pinte, C., et al. 2016, *Astronomy & Astrophysics*, 586, A103
- Zhu, Z., Hartmann, L., Gammie, C., & McKinney, J. C. 2009, *ApJ*, 701, 620
- Zubko, V., Kreiowski, J., & Wegner, W. 1996, *Monthly Notices of the Royal Astronomical Society*, 283, 577